Research Square

Preprints are preliminary reports that have not undergone peer review.
They should not be considered conclusive, used to inform clinical practice,
or referenced by the media as validated information.

Injectable Hydrogel-Integrated DNA-Programmed Mitochondrial Engagers Metabolically Rewire Synovial Macrophages for Osteoarthritis Repair

Maohua Chen
Army Medical Universit
Fengling Wang
Army Medical Universit
Xinqiang Hu
Chongqing University
Zhenqiang Wang
Army Medical Universit
Hao Wei
Chongqing University
Ming Qin
Army Medical Universit
Rong Huang
Army Medical Universit
Qing Luo
Army Medical Universit
Zhong Luo
Chongqing University
Jingbin Huang
sige@tmmu.edu.cn

Army Medical Universit

Research Article

Keywords: Osteoarthritis, DNA-Programmed Mitochondrial Engagers, Mitochondrial Fusion, Macrophages Repolarization, Metabolic Reprogramming

Posted Date: November 2nd, 2026

DOI: https://doi.org/10.21203/rs.3.rs-11108447/v1

License: This work is licensed under a Creative Commons Attribution 4.0 International License.
Read Full License

Additional Declarations: No competing interests reported.

Abstract

Mitochondrial dysfunction is a hallmark of synovial macrophages (SMs) in osteoarthritic joints, where it critically disrupts metabolic homeostasis in macrophages to promote pro-inflammatory activation, thereby driving OA-associated inflammation, oxidative stress, and cartilage matrix degradation. Herein, we developed an SM metabolic reprogramming strategy to reverse OA-associated osteochondral damage, emphasizing a supramolecular DNA-programmed mitochondrial engager (SDME) that selectively rejuvenates damaged mitochondria by harnessing the endogenous mitochondrial fusion-dependent repair program. SDME was synthesized through the self-assembly of bivalent cytochrome C-binding aptamer (DNA1) with a guanosine triphosphate (GTP)-releasing aptamer (DNA2). To improve the therapeutic performance of SDMEs in the complex osteoarthritic joint cavity, they were integrated with antioxidant quercetin (Qu) into biomineralized $CaCO_3$ nanosubstrates (BMRN) and further embedded into injectable gelatin/sodium alginate oxide-based hydrogel matrix (IHD). BMRNs were gradually released from the hydrogels following intraarticular injection and taken up by macrophages to deliver SDMEs and Qu-Ca complexes. By competitively binding Cyt-C on dysfunctional mitochondria, SDMEs bring the organelles into close proximity and synchronically release GTP to activate mitofusin-mediated mitochondrial fusion, which cooperates with Qu-Ca-mediated mitochondrial ROS scavenging to enable robust mitochondrial restoration, thereby metabolically reprograming pro-inflammatory macrophages toward a regenerative phenotype for efficient osteochondral healing. Overall, this study proposes a perspective OA treatment strategy through engager-directed mitochondrial rejuvenation.

1. Introduction

Osteoarthritis (OA) is a debilitating chronical joint disease prevalent among the elderly population, characterized by chronic synovitis and cartilage degeneration[1]. OA patients typically experience severe pain, abnormal bone remodeling, and persistent inflammation, all of which markedly reduce quality of life[2]. The pathological progression of OA is closely associated with the excessive activation and accumulation of pro-inflammatory synovial macrophages (SMs), which substantially impair chondrocyte function and induce chondrocyte apoptosis by secreting inflammatory cytokines[3, 4]. Indeed, macrophage phenotypes are directly correlated with OA severity and long-term prognosis in the clinic[5], highlighting the substantial therapeutic potential of SM reprograming for repairing OA-associated osteochondral damage and reversing disease progression. Clinical evidence increasingly implicates mitochondrial dysfunction as a central driver of SM maladaptation in OA conditions[6]. Notably, the osteoarthritic joint microenvironment markedly disrupts mitochondrial architecture and bioenergetic capacity, enforcing a metabolic transition from oxidative phosphorylation to glycolysis that sustains inflammatory macrophage activation[1, 7, 8]. Restoring mitochondrial fitness in SMs may therefore re-establish metabolic homeostasis to promote the pro-regenerative reprogramming of macrophages, offering significant promise to alleviate OA-associated osteochondral degeneration.

Nevertheless, despite the immense therapeutic promise, the pharmacological repair of dysfunctional SM mitochondria remains challenging. OA joints are characterized by persistent oxidative stress,

inflammatory cytokine accumulation, matrix-degradation products, hypoxia, acidic stress, and abnormal mechanical loading, all of which continuously impair the structural and functional integrity of mitochondria in resident SMs[2, 9–11]. Under hostile osteoarthritic conditions, conventional mitochondrial interventions such as antioxidants, metabolic regulators and mitochondrial transplantation often provide incomplete or transient benefits due to insufficient capacity to restore the mitochondrial network[12, 13]. Notably, healthy mammalian cells possess an integrated arsenal of mitochondrial quality-control and repair programs to preserve mitochondrial fitness under stress conditions including mitochondrial biogenesis, mitophagy and fission-fusion dynamics[14]. Interestingly, mitochondrial fusion represents a particularly important repair mechanism as it enables damaged mitochondria to merge with functional mitochondrial networks and facilitate the exchange of membranes, proteins, metabolites and mitochondrial DNA, thereby diluting mitochondrial defects and facilitating the restoration of mitochondrial health[15–17]. However, these endogenous repair programs are frequently compromised in OA-affected SMs by factors such as persistent oxidative stress and inflammatory cytokine signaling, which profoundly impair mitochondrial dynamics and shift the balance toward fragmentation, depolarization and glycolytic inflammatory polarization[18, 19]. Therefore, restarting mitochondrial fusion could reactivate the macrophage-intrinsic repair program to restore mitochondrial network integrity, emerging as a promising approach to achieve more durable pro-regenerative SM reprograming. Nevertheless, strategies that harness mitochondrial fusion for SM-targeted OA therapy remain underexplored, largely owing to the difficulty of selectively targeting dysfunctional mitochondria and delivering fusion-promoting cues to the appropriate intracellular sites.

To address these limitations, here we report a mitochondrial fusion-promoting strategy to reprogram macrophages for reversing OA-associated osteochondral damage. A bivalent Cyt-C-specific supramolecular DNA construct (SDME) was engineered for selectively bridging Cyt C on mitochondria and promoting their fusion-dependent rejuvenation programs. Taking advantage of the intrinsic biocompatibility and tailorability of DNA biomaterials, the SDME system was constructed by self-assembling two rationally engineered DNA components including DNA1 and DNA2. DNA1 presents two terminal Cyt C-binding aptamer domains, whereas DNA2 partially hybridizes with DNA1 to form a stable duplex while retaining a functional GTP aptamer module for GTP loading. Upon binding to mitochondrial Cyt C, the higher Cyt C affinity of DNA1 triggers structural rearrangement to liberate DNA2, which subsequently undergoes intramolecular hybridization to trigger GTP release. Consequently, SDMEs employ bivalent Cyt C engagement to tether damaged mitochondria in SMs while simultaneously releasing GTP to activate Mfn1, thereby coordinating mitochondrial apposition and fusion activation for efficient mitochondrial rejuvenation. Given the unfavorable pharmacokinetic profiles of DNA-based biomaterials in vivo, SDMEs were further biomineralized into $CaCO_3$ nanostructures with quercetin (Qu) to yield physiologically stable nanoplatforms (BMRNs) and subsequently incorporated into an injectable hydrogel matrix composed of oxidized sodium alginate (OSA) and gelatin. After intra-articular administration, gradual degradation of the OSA/gelatin hydrogel in the osteoarthritic joint cavity enabled sustained release of BMRNs, which could be preferentially internalized by SMs owing to their size-selective phagocytic capacity, where they released SDMEs and Qu-Ca complexes for coordinated

mitochondrial intervention. Mechanistically, SDMEs activated mitochondrial fusion, whereas Qu-Ca complexes scavenged mitochondrial ROS, collectively reinforcing mitochondrial quality control and restoring mitochondrial fitness. The BMRN-mediated cooperative mitochondrial rejuvenation shifted SM bioenergetic metabolism from glycolysis toward oxidative phosphorylation, thereby reprogramming them into a pro-regenerative phenotype to effectively attenuate joint inflammation and promote osteochondral repair. Overall, this study offers a promising mitochondrial rejuvenation strategy for improving OA treatment in the clinic.

2. Experimental Section

2.1 Materials

ALP assay kit, BCA assay kit, ROS detection kit and mitochondrial membrane potential detection kit were purchased from Beyotime Biotechnology Co. Ltd (China). Anhydrous calcium chloride, quercetin (Qu) and gelatin were purchased from Sigma-Aldrich. Sodium alginate (SA) and sodium periodate ($NaIO_4$) were purchased from Aladdin Co. Ltd (China). All primary antibodies were purchased from Abcam Co. Ltd (UK). Dulbecco's Modiffed Eagles Medium was obtained from Basalmedia Co. Ltd (China). Other reagents were purchased from Chuandong Chemical Company (Chongqing, China). OCR and ECAR assay kit were purchased from Agilent Technologies.

2.2 Preparation of BMRNs

The preparation of biomineralized nanostructures containing Qu was performed to previous studies[20]. Briefly, 150 mg of anhydrous calcium chloride with or without Qu (100 mg) were dissolved in 100 mL of ethanol containing 0.5 mL of deionized water to prepare SDME-free biomineralized nanoparticles (with Qu) and blank nanoparticles (without Qu). Subsequently, the solution was transferred into a glass bottle, which was then placed a sealed container filled with CO_2 and maintained at 30°C for 36 hours. The product was collected by centrifugation at 11000 rpm and washed twice with ethanol to obtain purified SDME-free biomineralized nanoparticles (SF-BMN) and blank nanoparticles (BN).

The SDME including DNA1 and DNA2, DNA1 aptamer exhibited high affinity to Cyt C, and DNA2 aptamer functioned as the GTP carrier due to its high affinity to GTP. A mixture of DNA1 (10 μM) and DNA2 (10 μM) were heated at 95°C for 5 min. After cooling to room temperature, GTP was added to the mixture, and it was maintained at 37°C for 2 hours to obtain SDME. Finally, the SF-BMN and SDME (100 nM) were incubated at 37°C for 2 hour and lyophilized at -80℃ to obtained biomineralized mitochondrion-rejuvenating nanoplatform (BMRN).

Fluorescence cross-correlation spectroscopy (FCCS) was used to characterize the combination of DNA1 and DNA2. FCCS cross-correlates two independent fluorescence signals that originate from two spectrally non-overlapping fluorescent labels that are attached to two distinct species. DNA1 was labeled with Alexa Fluor 488, and DNA 2 was labeled with Alexa Fluor 647. When this two fluorescence are not physically bound to each other, they will diffuse independently through the focal volume, thereby

generating distinctly different fluorescence intensity signals. The derived cross-correlation function exhibits a low amplitude, which, for FCCS measurements, is directly proportional to the degree of binding or colocalization. Whenever the Alexa Fluor 647- and Alexa Fluor 488-labeled DNA chains are bound to each other, their diffusion through the focal volume is coupled. Consequently, the generated spectrally distinct fluorescence signals show similar temporal fluctuations, resulting in a correlation function with a high amplitude. The degree of binding or colocalization for a sample containing Alexa Fluor 488- and Alexa Fluor 647-labeled species can be derived from the generalized definitions of the cross-correlation functions (Fcross), which is calculated by: F$cross$=max{$G_x(0)/G_A(0)$, $G_x(0)/G_B(0)$}, is Alexa Fluor 488, B is Alexa Fluor 647, x is cross yields the cross-correlation Gcross(τ).

Transmission electron microscope (TEM), dynamic light scattering particle sizer (Malvern) and zeta potential analyzer (Malvern) were employed to characterize the morphology, size, surface potential of BMRN nanoparticles.

2.3 Preparation of injectable hydrogels

The OSA was obtained by oxidation with $NaIO_4$. Briefly, $NaIO_4$ was added to SA (2%, w/v) solution, which was stirred at 60°C for 48 hours. Subsequently, the sample was dialyzed for 3 days using a 1500 Da dialysis membrane and lyophilized by vacuum freezing dryer. The obtained sample was oxidized sodium alginate (OSA).

The solutions of gelatin (20%, w/v) and OSA (2%, w/v) were mixed in a 1:1 ratio, and the transglutaminase (50 mg/mL) was added into the mixture to obtain the samples named Gel. For the loading of nanoparticles, BN, SF-BMN and BMRN were added into the mixture of gelatin, OSA and transglutaminase at a concentration of 2 mg/mL. The samples were denoted as hydrogel with blank nanoparticles (HBN), SDME-free biomineralized hydrogel (SF-BM), BMRN loaded injectable hydrogel depots (IHD), respectively.

2.4 Characterization of injectable hydrogels

Different cylindrical hydrogel samples with a diameter of 10 mm and a heigh of 6 mm were employed for mechanical tests. The compressive modulus of the samples was tested at a rate of 4 mm/min at a temperature of 37°C using a mechanical testing system (IBTC-ST05, Kaier, China). The elastic modulus was calculated from the linear region of the stress-strain curve for all samples.

A silicon nitride ceramic ball with a diameter of 3 mm was set to perform circular motion on the surfaces of different samples at a speed of 60 r/min, and the average load was 2 N. Cylindrical hydrogel samples with a diameter of 30 mm and a height of 4 mm were immersed in PBS at 37°C to test the friction property, and the test duration was 60 min.

2.5 Swelling of hydrogels

The injectable hydrogels (300 μL) were dried by vacuumed and weighed (M0) before being incubated with PBS in 37℃, and the PBS was replaced every day. At predetermined time intervals, the weight (Wt)

of the samples was measured, and the swelling ratio was calculated as:

$$SW = \frac{\mathrm{M}t - M0}{\mathrm{M0}} \times 100\%$$

2.6 Degradation of hydrogels

Gel, HBN, SF-BM, IHD were weighed (W_0) prior to incubation with PBS at 37°C, and the PBS was replaced daily. At predetermined time intervals, photographs of the hydrogel were taken to reflect the degradation of the sample. Meanwhile the weight (Wt) of the samples was recorded. The degradation of hydrogels was reflected by weight loss of hydrogel (W_{dr}) which was calculated by the formula: $W_{dr}=W_t-W_0$.

2.7 Release of Qu and SDME from the IHD

To explore the release kinetics of Qu and SDME from the hydrogels, IHD were immersed into 1 mL PBS. At different time intervals, the precipitate in the incubation solution was collected, and the incubation solution was replaced with fresh solution. Subsequently, 0.1 mM hydrochloric acid was added to dissolve the released BMRN, and high-performance liquid chromatography (HPLC) was used for detecting the release amount of Qu with a flow rate of 1.0 mL/min. The mobile phase of the HPLC consisted of methyl alcohol (49.75%), deionized water (49.75%), and phosphoric acid (0.5%), and the detection wavelength was set at 375 nm. The peak area at 6-7.5min was calculated to reflect the release amount of Qu. NanoDrop Microvolume was utilized to detect the release amount of SDME.

2.8 ROS scavenging ability of BMRNs

2,2-Diphenyl-1-picrylhydrazyl (DPPH) was used to measure the ROS scavenging capability of Qu-Ca complex. The BMRNs were mixed with DPPH solution (0.041 mg/mL) and incubation for 30 min at 37℃. The changes in absorbance at a wavelength of 519 nm were recorded to evaluate the ROS scavenging ability of BMRNs.

2.9 Detection of the SOD/CAT like catalytic activity of different samples

The SOD-like catalytic activity of BN, SF-BMN and BMRN were detected using an SOD assay kit (Beyotime) in accordance with the protocols. A working solution was prepared by mixing 7550 μL of the SOD detection buffer solution, 50 μL of the enzyme solution, and 400 μL of the water-soluble tetrazolium salt (WST-8) solution. were mixed to prepare the working solution. Subsequently, the incubation solutions of different Gel-based samples were added to the working solution and incubated at 37°C for 30 min. Finally, the absorbance at 450 nm was measured using microplate reader.

The CAT-like catalytic activity of different samples was detected by hydrogen peroxide detection kit (Beyotime). The BN, SF-BMN and BMRN were incubated with H_2O_2 (250 mM) for 5 min at 25°C. Subsequently, the stopping solution and color-developing solution were added sequentially, followed by

incubation for 30 min at 25°C. Finally, the absorbance at 520 nm was measured using a microplate reader.

2.10 Cell culture

Bone marrow macrophages (BMMs) were isolated from the femurs/tibias of OA and healthy Sprague-Dawley rats (SD rats) and cultured in high-glucose Dulbecco's Modiffed Eagle's Medium (DMEM) supplemented with 10% (v/v) fetal bovine serum (FBS), M-CSF (30 ng/mL), 1% penicillin-streptomycin at 37°C in a 5% CO_2 atmosphere. Chondrocytes were purchased from Anweisci Co. Ltd. (Shanghai, China) and cultured with high-glucose DMEM containing 10% (v/v) FBS, 1% penicillin-streptomycin at 37°C in a 5% CO_2 atmosphere.

2.11 Sample uptake in vitro

FITC (10 mg) was used to prepare BMRN-FITC nanoparticles and IHD-FITC. The uptake of BMRN-FITC by BMMs were visualized by confocal laser scanning microscopy (CLSM). Briefly, BMRN-FITC were loaded into IHD to prepare IHD-FITC samples, which were incubated with DMEM culture medium for 28 days. The incubation medium was collected at predetermined time points and utilized for culturing BMMs for 24 h. Subsequently, the cells were washed three times by PBS and fixed with 4% paraformaldehyde for 30 min at 4 ℃. The cell cytoskeleton and nuclei were stained with rhodamine-phalloidin and Hoechst 33258, respectively. Finally, the samples were observed by CLSM.

2.12 Cell viability assay

BMMs and chondrocytes were seeded on different hydrogels surface at a density of 2×10^4 cells/well and supplied with DMEM culture medium. After 7 days, fresh medium containing 10% cell counting kit-8 (CCK8) was added and incubated for 2 h at 37℃. The medium was subsequently transferred into a 96-well plate and detected at 450 nm by microplate reader. In addition, calcein/PI staining was used to reflect the number of live/dead cells after the BMMs and chondrocytes were cultured on different hydrogels surface. Finally, the samples were observed by CLSM.

2.13 Immunofluorescent staining

BMMs were cultured on Gel, HBN, SF-BM and IHD with LPS (5 μg/ mL) stimulation for 3 days. The samples were immobilized with 4% paraformaldehyde and permeabilized using 0.1% triton X-100, respectively. Then the samples were blocked with 5% BSA in PBS for 2 h before incubating with primary antibodies at 4℃ overnight. Afterward, the samples were treated with secondary antibodies and Hoechst 33258 for 1 h and 10 min at room temperature, respectively. Finally, fluorescent images were captured with CLSM.

2.14 Detection of intracellular ROS levels

BMMs cells were cultured on Gel, HBN, SF-BM and IHD with LPS (5 μg/ mL) stimulation for 3 days. Subsequently, the culture media were replaced with fresh serum-free media containing 2,7-Dichlorodi-hydroffuorescein diacetate (DCFH-DA, 0.1%). Then, the samples were incubated for 20 min at 37℃ and

washed three times with serum-free medium. Finally, FCM and CLSM were employed to examine the ROS levels in BMMs.

2.15 Detection of mitochondrial membrane potential

BMMs were cultured on different hydrogels with LPS (5 μg/ mL) stimulation for 3 days. Subsequently, the culture media were replaced with new ones containing JC-1 working solution (50% v/v). After incubation for 20 min at 37°C, the medium was replaced with fresh medium and observed with CLSM.

2.16 Evaluation of anti-inflammatory effects

BMMs were seeded on the surface of different hydrogels and cultured in 6-well plates with a density of 2×10^5 cells/well. The culture was supplied with DMEM culture media containing LPS (5 μg/ mL). After 3 days, the levels of inflammatory cytokines TNF-α and IL-6, as well as anti-inflammatory cytokines IL-10 and IL-4 were quantified using an ELISA kit (ThermoFisher) according to manufacturer's instructions. Moreover, BMMs were treated in the same manner, and macrophage polarization was analyzed by flow cytometry. After being washed three times with PBS, the cells were collected and incubated with antibodies against CD86 and CD206 for 30 min at room temperature. Subsequently, the samples were washed three times with PBS and detected using flow cytometry.

2.17 Transcriptomic and metabolomic analysis

BMMs were cultured on different hydrogels with LPS (5 μg/ mL) stimulation and used for transcriptomic analysis of the functionality of IHD hydrogel, which was conducted by Majorbio Co., Ltd. (Shanghai, China). BMMs were treated with TRIzol to extract RNA, and the NanoDrop 2000 and Agilent 5300 Bioanalyzer were used to measure the RNA content and integrity number. Subsequently, the sequencing experiment was carried out using the SMART-Seq V4 Ultra Low Input RNA Kit for Sequencing to construct the library. The transcriptome was sequenced and analyzed by Majorbio on the Illumina Novaseq 6000 platform. RNA purification, reverse transcription, library construction, and sequencing were all performed at Majorbio Co., Ltd. (Shanghai, China).

Metabolomic analysis of macrophages from different treatment groups was conducted by Majorbio Co., Ltd. (Shanghai, China). Macrophages were cultured on the surface of different hydrogels for 3 days, then collected via low-speed centrifugation (1200 rpm/min, 10 min, 4°C), flash-frozen in liquid nitrogen, and stored at -80°C. Subsequently, metabolite extraction and LC-MS analyses were carried out at Majorbio Co., Ltd, employing an Orbitrap Exploris 240 system Mass Spectrometer equipped with an electrospray ionization source. Raw spectral data were processed using Progenesis QI (Waters Corporation, Milford, USA) software, and a three-dimensional data matrix in CSV format was exported. Meanwhile, the metabolites were identified by searching databases, with the main databases being HMDB, Metlin, and the self-compiled Majorbio Database (MJDB) of Majorbio Biotechnology Co., Ltd. (Shanghai, China). Additionally, The R package "ropls" (Version 1.6.2) was used to perform principal component analysis (PCA) and orthogonal least partial squares discriminant analysis (OPLS-DA), as well as 7-cycle interactive validation to evaluate the stability of the model.

2.18 ATP detection

BMMs were cultured on the surface of different hydrogels for 3 days in the presence of LPS. The ATP level was detected using an ATP assay kit (Beyotime). After washing the cells three times with PBS, lysis buffer was added, and the cells were incubated for 10 min, followed by centrifugation at 12000g and 4°C for 5 min. Subsequently, 20 μL of the supernatant was mixed with 100 μL of ATP detection solution. Finally, fluorescence microplate reader was employed to measure the luminescence intensity of the mixture.

2.19 TEM analysis of macrophages

BMMs were cultured on the surface of different hydrogels for 3 days in the presence of LPS. Subsequently, the culture media were discarded, and the samples were washed three times with PBS. Thereafter, the cells were collected via centrifugation (1200 rpm/min) and immersed in 1 mL of 2.5% glutaraldehyde for 12 h at 4°C. The aggregated cells were dehydrated using acetone, embedded into epoxy resin, cut into ultrathin section with a thickness of 50 nm, and stained with both uranyl acetate and lead citrate. Finally, the subcellular structures were observed by TEM.

2.20 Chondrogenesis evaluation

BMMs were cultured on the surfaces of Gel, HBN, SF-BM and IHD, the medium was collected regularly for chondrocytes culturing. After culturing for 7 days, chondrocytes were fixed with 4% paraformaldehyde and stained with alcian blue for 2 hours. Subsequently, the samples were washed three times with deionized water and observed by optical micrographs. Moreover, the quantitative real-time PCR was employed to detect the expression of chondrogenesis-related genes (ACAN, Col Ⅱ, SOX9 and MMP13). Briefly, the RNA of chondrocytes was isolated in accordance with the instructions of the RNAiso Plus RNA Purification Kit (Takara) after 7 days of co-culturing with BMMs. Finally, real-time PCR was performed on the Bio-Rad CFX Manager system. The amplification conditions for cDNA were as follows: 95°C for 3 s, followed by 45 cycles at 95°C for 5 s, and then 60°C for 30 s.

2.21 Osteoclastogenesis evaluation

BMMs were cultured on different substrates, including Gel, HBN, SF-BM and IHD, and induced with M-CSF (25 ng/ml) and RANKL (50 ng/ml) for 7 days. For cell co-culture observation, cells were labeled with Hoechst or CM-Dil for 20 min at 37°C, then co-cultured for 24 h and visualized by CLSM. For cytoskeletal staining, cells were washed three times with PBS, fixed with 4% paraformaldehyde for 30 min at room temperature, and stained with rhodamine-labeled phalloidin for the cytoskeleton and DAPI for the nucleus before CLSM observation. For TRAP analysis, cells were washed three times with PBS and the tartrate-resistant acid phosphatase activity was measured using a TRAP assay kit (Beyotime) according to the manufacturer's instructions.

2.22 Establishment of the OA rat model and treatment

SD rats (male, weight 200 g) were obtained from Hunan SJA Laboratory Animal Co., Ltd. OA was induced by anterior cruciate ligament transection (ACLT) surgery. Briefly, following routine disinfection, the knee joints of the rats were exposed, and the anterior cruciate ligament was transected, followed by the removal of the anterior horn of the medial meniscus. After being fed for 4 weeks, the knee joints were injected with different hydrogels, including Gel, HBN, SF-BM and IHD. The OA rats were euthanized after another 8 weeks of injection of different hydrogels, and their knee joints were collected for analysis.

2.23 ROS detection in vivo

The ROS levels in the knee joint were detected via dihydroethidium (DHE) staining. Specifically, DHE was dissolved in DMSO and diluted with a solution containing 5% Tween-80, 5% polyethylene glycol 400, and 0.9% NaCl. Subsequently, the mixture was injected into SD rats via tail vein. After 24 hours, the rats were euthanized, and their knee joints were collected for fixation and decalcification using mixture solution containing 10% nitric acid and 15% methanol treatment for 24 hours. Afterwards, the samples were embedded in optimal cutting temperature (OCT) compound and longitudinally sectioned at a thickness of 5 μm. Finally, the red fluorescence in the knee joints was imaged by VS200 whole-slide scanning imaging system (Olympus).

2.24 Micro-CT

The OA rats were euthanized after being injected with different hydrogels for 8 weeks. Subsequently, the knee-joints were removed and fixed in 4% paraformaldehyde. Micro-CT was employed to assess the status of joint injury. Scans were conducted on a SCANCO micro-CT scanner to quantify the new bone volume per total volume (BV/TV), trabecular thickness (Tb.Th) and trabecular number (Tb.N). Regarding the three-dimensional micro-CT characterization of the extracted bone samples, the analysis scope was the rat knee joint, which is a standard setting for micro-CT analysis of OA treatment in previous reports.

2.25 Histological analysis

For histological staining, the samples were fixed with 4% paraformaldehyde for 48 hours and decalcified using 15% of ethylenediaminetetraacetic acid disodium salt (EDTA-2Na) for one month. The samples were treated with ethanol at graded concentrations, embedded in paraffin, and longitudinally sectioned at a thickness of 5 μm. The bone tissue slides were stained with hematoxylin-eosin (H&E), Masson’s trichrome (MT) and Safranin O/fast green to characterize the cartilage regeneration. Furthermore, immunohistochemical staining of matrix metallopeptidase 13 (MMP13), collagen Ⅱ (Col Ⅱ) and aggrecan (ACAN) was performed to analyze joint repair.

2.26 Statistical Analysis

All experiments were repeated 3 times, and the data are presented as mean values ± standard deviations. Statistical analysis was conducted by OriginPro (version 2021) via one-way analysis of variance (ANOVA) followed by Tukey's post hoc test. The confidence levels were set as 95% ($p < 0.05$) and 99% ($p < 0.01$).

3. Results and discussion

3.1 Mitochondrial metabolic signatures of OA-associated macrophages

Previous studies have shown that mitochondrial dysfunction in SMs is closely associated with the OA progression. Specifically, pro-inflammatory M1 macrophages generally exhibit impaired mitochondrial metabolism, characterized by a predominant reliance on glycolysis for ATP production and excessive generation of reactive oxygen species (ROS)[6, 14]. In contrast, anti-inflammatory M2 macrophages predominantly depend on OXPHOS to meet the bioenergetic demands, which requires intact mitochondrial structure and efficient electron transport across the inner mitochondrial membrane. Indeed, mitochondrial homeostasis has been widely recognized as a key determinant of SM polarization and the associated inflammatory responses in OA pathology. Here we established an OA rat model (Figure S1A) and extracted BMMs to examine their mitochondrial characteristics. As shown in Figure S1B, BMMs from OA rats exhibited pronounced mitochondrial structural damage including severely compromised mitochondrial membrane integrity, reduced number of cristae per mitochondrion, and decreased cristae density. Together, these observations support the hypothesis that the loss structural and functional integrity of mitochondria is a hallmark in OA-affected BMMs and plays a crucial regulatory role in determining macrophage polarization during OA progression.

3.2 Preparation and characterization of BMRNs

SDMEs were fabricated through the spontaneous self-assembly of two rationally designed DNA strands (DNA1 and DNA2) in an aqueous solution, which were synthesized through complementary base pairing. FCCSs analysis immediately confirmed the chemical composition and conformation of the DNA components. Specifically, DNA1 contains Cyt C aptamer domains at both termini with a six-nucleotide core sequence of the GTP-binding aptamer in the central region. Meanwhile, DNA2 contains terminal sequences partially complementary to the Cyt C aptamer domains of DNA1 at both ends, which were connected to two short domains complementary to the GTP-binding aptamer core sequence, and a complete-binding GTP aptamer sequence in the center for GTP loading. The complementary regions between DNA1 and DNA2 comprise 14 base pairs, allowing the formation of a stable duplex structure. Notably, the Cyt C-responsiveness of the resulting SDMEs are achieved through competitive binding of Cyt C to DNA1 to displace DNA2 segments, as DNA1 exhibits higher affinity for Cyt C than for the complementary regions of DNA2. The dissociated DNA2 subsequently undergoes intramolecular hybridization, in which the complementary domains bind to the core region of the GTP-binding aptamer and occupy the GTP-binding site, thereby attenuating the interaction between the aptamer and GTP to trigger GTP release (Scheme 1).

Previous investigations have demonstrated that Qu can form stable coordination complexes with Ca^{2+}, thereby facilitating its incorporation into biomineralized nanoparticles [21]. Based on this approach, we successfully synthesized SF-BMN via the established CO_2 diffusion method[22, 23]. On account of the

strong affinity of Ca^{2+} for the phosphate groups in DNA components, SDME was loaded onto nanoparticle surface to yield BMRN. As shown in Fig. 1A, BMRN maintains a spherical structure similar to BN and SF-BMN nanoparticles, exhibiting a uniform distribution of Ca, O, P, and C elements (Fig. 1B). Dynamic light scattering (DLS) analysis revealed that the diameter of BN nanoparticles was approximately 80 ± 3.6 nm, which increased significantly to 200 ± 5.6nm and 220 ± 3.1 nm after Qu and SDME loading, respectively (Fig. 1C). Concurrently, the zeta potential of SF-BMN increased markedly from − 18.3 mV to -13.9 mV, which can be attributed to the incorporation of Qu. During this process, partial substitution of CO_3^{2-} by Qu may occur through coordination with Ca^{2+}, thereby reducing the overall negative surface charge. Subsequent loading of the negatively charged SDME further decreased the zeta potential to -22.5 mV due to the abundant phosphate groups. (Fig. 1D). Quantitative analysis by HPLC and UV-vis spectrophotometry showed that the loading ratios (w/w) of Qu and SDME were 10.4% and 0.8%, respectively (Fig. 1F). Agarose gel electrophoresis consistently demonstrated that the maximal SDME by SF-BMN was around 100 nmol of SDME per 1 mg of SF-BMN (Fig. 1G).

Excessive ROS production by M1-like macrophages is a key contributor to OA progression as it not only reinforces synovial inflammation but also induces persistent mitochondrial damage to accelerate cartilage degeneration[5, 11]. Thus, local ROS scavenging within the joint cavity is crucial for enabling durable OA amelioration. For this purpose, the clinically approved antioxidant Qu was coordinated with Ca^{2+} during biomineralization to yield stable Qu-Ca complexes (Fig. 1K). ^1H NMR analysis revealed a distinct shift of the phenolic hydroxyl proton of Qu in SF-BMN relative to free Qu, confirming the coordination between Qu and Ca^{2+} (Figure S2). Interestingly, coordination with Ca^{2+} ions significantly enhanced the antioxidant performance of Qu. According to the results of radical scavenging assays, both SF-BMN and BMRN nanoparticles eliminated approximately 60% of DPPH radicals and 70% of H_2O_2, which was evidently superior to pristine Qu and could be explained by the multi-enzyme-mimetic activity of the Qu-Ca complex (Fig. 1H, I). Enhanced activity may be associated with the formation of redox-active Qu-Ca coordination sites with enzyme-mimetic catalytic properties. Indeed, SF-BM and IHD significantly suppressed formazan formation (Fig. 1J), demonstrating efficient SOD-like activity for catalyzing superoxide anion dismutation. To further elucidate the molecular mechanism underscoring the enhanced antioxidant activity of Qu-Ca complexes, DFT simulations were performed using the proposed Qu-Ca configuration, which affirmed the strong adsorption of the Qu-Ca complexes toward typical ROS species with adsorption energies of -1.04 eV for $\cdot O_2^-$, -1.59 eV for ·OOH, -2.48 eV for H_2O_2, and − 3.36 eV for ·OH (Figure L, M and S4), indicating its capacity to capture and stabilize pro-degenerative radicals. Simulation modeling further revealed that Qu-Ca interacted more intimately with key ROS intermediates than free Qu, supporting more efficient radical conversion. These results indicate that Ca^{2+} coordination enhances the ROS engagement and elimination capability of Qu for endowing superior antioxidative activities.

3.3 Preparation and Characterization of IHDs

Injectable hydrogels are promising delivery platforms for OA therapy on account of their biodegradability, lubrication capacity, local retention, and sustained-release properties, which are highly desirable for

prolong drug retention in the joint cavity while reducing systemic exposure[24, 25]. In this study, the as-prepared BMRN nanoparticles were integrated into gelatin/OSA hydrogel matrices to improve their pharmacokinetic performance. For this purpose, oxidized sodium alginate (OSA) was first synthesized through oxidation with sodium periodate, of which the successful preparation was validated by ^{1}H NMR spectrum (Figure S5B) and Fourier transform infrared spectroscopy (FTIR) analysis (Figure S5C). The generated OSA subsequently reacted with gelatin via dual crosslinking by dynamic Schiff base reaction and transglutaminase (TG) ligation. The morphology of the resulting hydrogels was first examined by SEM. The Gel samples exhibited a homogeneous porous network with a porosity of approximately 40%. After incorporation of BN, SF-BMN and BMRN nanoparticles, the overall porous architecture was well preserved, indicating that nanoparticle loading did not disrupt hydrogel network formation (Fig. 2B, C). Contact angle measurements further showed that nanoparticle incorporation imposed negligible influence on hydrogel surface hydrophilicity, for which all groups presented similar contact angles at approximately 60° (Fig. 2D). The hydrogels also displayed excellent injectability, as they could be smoothly extruded through a syringe needle and rapidly recovered to a gel state in PBS (Fig. 2J). Owing to dynamic crosslinked network, the IHD hydrogels also showed robust self-healing capacity. Interfacial diffusion and bond reformation occurred within 30 min after bringing two separate hydrogel pieces into close contact, resulting in complete macroscopic fusion. SEM observation of the healed cross-section further revealed no obvious boundary at the contact interface despite slight differences in micro-orientation between the two hydrogel pieces (Fig. 2K). The self-healing mechanism was attributed to the intrinsic reversibility of the multivalent interactions including Schiff base bonds and hydrogen bonding between OSA and gelatin.

The mechanical properties of the IHD hydrogel were comprehensively tested. Compression testing (Fig. 2F-H) indicates that the elastic modulus of the Gel is approximately 0.14 MPa, which is lower than native cartilage and therefore will not trigger cartilage abrasion after injection. Loading with BN, SF-BMN, or BMRN nanoparticles did not significantly alter the elastic modulus or the area under the compression (AUC) curve, suggesting that nanoparticle incorporation imposed minimal effect on the overall stiffness and compressive behavior of the hydrogel. Moreover, cyclic compression tests conducted at a maximum strain of 60% for 20 cycles showed negligible energy dissipation and no obvious permanent deformation, indicating excellent elastic recovery and structural stability (Fig. 2I). The excellent fatigue resistance can be attributed to the reversible dissociation and reformation of dynamic Schiff base bonds and hydrogen bonding in response to the mechanical stress, which is particularly important for intra-articular applications as it allows the hydrogel to maintain structural integrity during routine joint motion and provide a stable depot for sustained nanoparticle release.

Joints constantly experience complex motion during daily activities, enforcing continuous friction between articular cartilage and intra-articular materials. Therefore, adequate lubrication is essential for hydrogel implants designed for joint applications, as low-friction interfaces can reduce mechanical wear on cartilage and subchondral bone. To evaluate the tribological performance of the hydrogels under joint-relevant conditions, sliding friction tests were performed in PBS at 37°C. Considering that normal knee flexion-extension during walking occurs at approximately 0.5 Hz as well as the reduced physical

activity in OA patients, a sliding frequency of 0.5 Hz was selected to mimic the joint motion under OA conditions. Under a 2 N load, the Gel group showed the lowest friction coefficient at approximately 0.03 (Fig. 2L, P). Incorporation of BN, SF-BMN, or BMRNs slightly increased the friction coefficient, but the changes were not statistically significant. Importantly, the friction coefficients for all hydrogels were below 0.05, which were comparable to the lubricating performance of native articular cartilage. These results indicate that IHD possesses excellent interfacial lubrication capacity for reducing mechanical wear after intra-articular administration, which is particularly important for OA patients with impaired osteochondral functions.

Finally, the in vitro degradation and release profiles of IHD hydrogels were investigated. In PBS at 37°C, the hydrogels showed gradual weight loss owing to the intrinsic degradability of both OSA and gelatin. Approximately 50% of the hydrogel mass remained after 14 days, which further decreased to about 10% remained after 28 days. No significant differences in degradation behavior were observed among the different hydrogel groups (Fig. 2E). It is also important to note that BMRN nanoparticles were progressively released along with hydrogel degradation and subsequently dissociated under mildly acidic conditions to liberate Qu and SDME. The cumulative release of Qu and SDME was quantified by HPLC and UV-vis spectrophotometry, respectively. Over 28 days, the cumulative Qu release reached approximately 98 μg, corresponding to an average daily release of around 3.5 μg/mL (Fig. 2N). The daily SDME release was approximately 317 ng/mL, showing a stable sustained-release profile (Fig. 2O). Interestingly, the diameter and zeta potential of the hydrogel encapsulated nanoparticles including BN, SF-BMN and BMRN showed no obvious changes under physiological conditions over a period of 21 days, immediately suggesting the nanoparticle stabilizing effect of the hydrogel matrix (Fig. 1E and S3B). These results indicate that the OSA/gelatin hydrogel can serve as a long-term intra-articular depot for the sustained and stable delivery of Qu and SDME-loaded nanoparticles.

3.4 Uptake and biocompatibility analysis of IHD

To evaluate the biocompatibility of IHD, typical joint-residing cell populations including BMMs and chondrocytes were cultured on the surfaces of Gel, HBN, SF-BM and IHD hydrogels for 7 days. CCK-8 assays and live/dead staining consistently revealed no obvious cell death in all groups, demonstrating the excellent cytocompatibility of these hydrogel samples (Fig. 3A, C and Figure S6). Meanwhile, to further elucidate cellular uptake dynamics, FITC-labeled BMRN nanoparticles were incorporated into hydrogels and subsequently immersed in culture media. The incubation solution was collected at predetermined intervals to culture BMMs. As shown in Fig. 3B and D, the intracellular green fluorescence signal in BMMs did not change significantly in 7, 14 and 21 days of co-culturing with the IHD-FITC immersion solution, suggesting BMRN nanoparticles were slowly released from hydrogels and internalized by macrophages. The macrophage uptake and intracellular trafficking of BMRN-FITC nanoparticles were then investigated by examining their subcellular colocalization with lysosomes in BMMs. After 3 hours of incubation, BMRN-FITC nanoparticles showed substantial overlap with LysoTracker Red-labeled lysosomes to yield strong orange fluorescence, indicating that the nanoparticles were internalized by BMMs mainly through the endocytic pathway in line with previous

reports. Interestingly, after 8 h of incubation, the green fluorescence became clearly separated from the red lysosomal signal, suggesting successful lysosomal escape of BMRN-FITC nanoparticles (Fig. 3E).

To investigate the mitochondrion-targeting ability of the SDMEs, both the 3' and 5' ends of the Cyt C aptamer were labeled with FAM to prepare BMRN-FAM for in vitro tracking. After hydrogel immersion in culture medium, the release solution was collected for culturing BMMs. After 8 h, strong colocalization between green fluorescence (SDMEs) and red fluorescence (mitochondria) was observed, indicating that the released SDMEs could selectively bind to mitochondria through Cyt C-aptamer complexation (Fig. 3F). Interestingly, IHD treatment induced efficient mitochondrial fusion in M1-like macrophages according to mitochondrial ultrastructure analysis (Fig. 3G). Contrasting the obvious mitochondrial damage in the Gel and HBN groups including mitochondrial swelling, disrupted outer membranes, cristae dissolution, and pronounced fragmentation, mitochondria in the BMRN group displayed healthy morphologies including continuous, rounded, and tubular morphologies with well-defined cristae, indicating enhanced mitochondrial restoration thereof. Interestingly, the macrophage mitochondria in the IHD group presented the typical damage-associated fragmented morphology at 0 h but became aggregated into an elongated morphology after 8 h of culture, demonstrating its ability to rapidly promote mitochondrial fusion via SDME-mediated proximity effects in M1-like macrophages (Fig. 3H).

3.5 Evaluation of SDME-mediated mitochondrial fusion

We next investigated if the released SDMEs could promote mitochondrial fusion through cooperative physical bridging and the Cyt C-responsive GTP release. Meanwhile, the Cyt C-triggered structural switching of DNA1 and the associated GTP release were investigated using fluorescence cross-correlation spectroscopy (FCCS) by monitoring the co-diffusion of dual-labeled DNA strands[26, 27]. For this purpose, DNA1 and DNA2 were labeled at their 3' termini with Alexa Fluor 488 and Alexa Fluor 647, respectively. After incubation at 37°C for 2 h, the cross-correlation amplitude G(τ) increased to 0.56, indicating stable hybridization between DNA1 and DNA2 with a dissociation constant of 136.06 nM (Fig. 4B). In comparison, DNA1 showed stronger affinity for Cyt C with a K_D of 21.7 nM, while DNA2 bound to GTP with a K_D of 85.8 nM (Fig. 4C, D). To determine whether Cyt C could trigger duplex dissociation, we further measured the interaction between the SDMEs and Cyt C. The SDMEs-Cyt C interaction exhibited a K_D of 104 nM, supporting the ability of Cyt C to competitively bind DNA1 and displace DNA2 from the duplex. Indeed, Cyt C induced efficient dissociation of the DNA1/DNA2 duplex in a concentration-dependent manner, evidenced by the gradual decrease in Fcross values with increasing Cyt C concentration (Fig. 4E, F). At 70 nM Cyt C, the duplex was almost completely dissociated, while even 10 nM Cyt C was sufficient to initiate obvious strand separation (Fig. 4G). Following Cyt C-triggered dissociation, DNA2 underwent intramolecular base pairing that disrupted its GTP-binding pocket, resulting in efficient GTP release (Figure S8C). In line with the observations above, SDME treatment induced efficient mitochondrial fusion in M1-like macrophages according to mitochondrial ultrastructure analysis. Together, these results demonstrate that SDME acts as a multifunctional mitochondrial engager that selectively bridges dysfunctional Cyt C-positive mitochondria while synchronically releasing

GTP to activate the Mfn1 signaling, thereby directing mitochondrial fusion for promoting mitochondrial rejuvenation in stressed BMMs.

3.6 In vitro ROS scavenging by BMRN nanoparticles

OA pathology is marked by the accumulation of excessive M1-like macrophages generating abundant ROS, which promotes chondrocyte apoptosis and accelerates articular cartilage degeneration[28, 29]. Therefore, we investigated if the Qu-Ca complex in BMRN could eliminate ROS in pro-inflammatory macrophages. Here the BMMs were inoculated onto various hydrogels, and the intracellular ROS levels were detected using the DCFH-DA probe (Fig. 4H and Figure S7). Compared with the Gel and HBN groups, SF-BM and IHD groups showed markedly reduced intracellular ROS levels, which can be attributed to the SOD-like and CAT-like activities of the Qu-Ca complex. As excessive ROS directly impairs mitochondrial function, we further assessed mitochondrial membrane potential using the JC-1 probe. In healthy mitochondria with high membrane potential, JC-1 forms aggregates and emits red fluorescence, whereas mitochondrial depolarization results in green fluorescence. As shown in Fig. 4I, macrophages cultured on SF-BM and IHD surfaces displayed strong red fluorescence and weak green fluorescence that indicates successful preservation mitochondrial membrane potential. Contrastingly, the trends were reversed in the Gel and HBN groups, suggesting pronounced mitochondrial depolarization. These results indicate that the Qu-Ca complex effectively alleviates oxidative mitochondrial damage by efficient ROS scavenging to maintain mitochondrial membrane potential.

3.7 IHD reprograms mitochondrial bioenergetics in macrophages

To investigate if the IHD-mediated reparation of dysfunctional mitochondria could rewire macrophage bioenergetics, seahorse extracellular flux analysis was performed to measure the oxygen consumption rate (OCR) and extracellular acidification rate (ECAR) of LPS-stimulated BMMs cultured on different hydrogel surfaces. Compared with the Gel and HBN groups, BMMs cultured on SF-BM and IHD exhibited markedly increased maximal respiration, spare respiratory capacity, and ATP production, indicating enhanced mitochondrial respiration following specific treatment (Fig. 4J-L and Figure S9). On the other hand, ECAR analysis showed significantly reduced glycolytic capacity and glycolytic reserve in the SF-BM and IHD groups, suggesting suppressed glycolytic metabolism (Fig. 4M-O). Together, these OCR and ECAR results demonstrate that IHD markedly shifts macrophage bioenergetics from glycolysis toward OXPHOS. To further elucidate the molecular basis of IHD-induced metabolic rewiring, integrated transcriptomic and spatial metabolomic analyses were performed using BMMs cultured on different hydrogel surfaces[30].

Principal component analysis of spatial metabolomic data showed good reproducibility within each group and clear separation among groups, indicating distinct metabolic profiles for different hydrogel formulations (Fig. 5A). Compared with the Gel group, the IHD group displayed broad metabolic remodeling, with 501 metabolites significantly upregulated and 327 downregulated (Fig. 5B). Venn

analysis further identified 281 shared differentially expressed metabolites across all groups (Fig. 5C). Notably, heatmap analysis revealed enrichment of TCA cycle-associated metabolites, including isocitrate, malate, and succinate, together with elevated levels of key metabolic enzymes such as isocitrate dehydrogenase 3 gamma (IDH3G) and citrate synthase (CS) (Fig. 5D). Consistently, KEGG enrichment analysis indicated that these metabolic alterations were mainly involved in the TCA cycle, oxidative phosphorylation, starch/sucrose metabolism, and AMPK signaling pathways (Fig. 5E). Integrated transcriptomic and metabolomic analyses further identified 28 metabolism-related genes mainly involved in AMPK signaling, the TCA cycle, oxidative phosphorylation, and fructose/mannose metabolism (Fig. 5F, G). Consistently, GSEA showed that IHD activated TCA cycle and oxidative phosphorylation gene sets, while suppressing glycolysis and osteoclast differentiation pathways (Fig. 5H-K). These results suggest that IHD promotes mitochondrial metabolism while limiting glycolytic and osteoclastogenic programs.

In line with the transcriptomic and spatial metabolomic results above, metabolic profiling further confirmed that BMMs cultured on IHD preferentially utilized the TCA cycle and OXPHOS for energy production, whereas cells in the Gel group relied primarily on glycolysis (Fig. 5L). Moreover, metabolite-gene interaction network analysis revealed close associations between typical TCA cycle intermediates (fumarate, malate, succinate, citrate, and isocitrate) and genes involved in inflammation regulation, antioxidant defense, and macrophage polarization (IL-10, IL-6, TNF, TGF-β, SOD, NAD-related enzymes, and GPX4) (Fig. 5M). These results suggest that mitochondrial metabolic intermediates have substantial impact on macrophage polarization to regulate the associated inflammation responses. Collectively, the multi-omics data demonstrate that IHD restores mitochondrial function and rewires macrophage bioenergetics from glycolysis toward oxidative phosphorylation.

3.8 IHD metabolically modulates macrophage polarization

To investigate whether IHD-mediated metabolic rewiring could regulate macrophage polarization, RNA-seq analysis was performed on LPS-stimulated BMMs cultured on different hydrogel surfaces. Compared with the Gel group, the IHD group showed 1,403 upregulated genes and 1,730 downregulated genes (Fig. 6A). Among these differentially expressed genes, anti-inflammatory and tissue-reparative markers including IL4, IL10, and TGF-β were markedly upregulated, whereas pro-inflammatory genes including IL-1β, TNF, and IL12 were significantly downregulated (Fig. 6C). GO and KEGG enrichment analyses further showed that JAK-STAT6, PI3K-Akt, and TGF-β/Smad signaling pathways were enriched in the IHD group, immediately suggesting the successful macrophage repolarization toward a pro-regenerative M2-like phenotype (Fig. 6D, E). In addition, pathways related to metabolism, immune regulation, and signal transduction were significantly enriched (Figure S10), further supporting the capacity of IHD to drive pro-regenerative macrophage phenotypic transition through metabolic rewiring. Consistent with the RNA-seq results, flow cytometry and immunofluorescence staining results showed that SF-BM and IHD significantly reduced the proportion of $CD80^+$ cells while increasing the proportion of $CD206^+$ cells compared with the Gel group (Fig. 6F-I), again validating the treatment-induced macrophage repolarization from an M1-like phenotype toward an M2-like phenotype. ELISA analysis

further demonstrated that LPS-stimulated macrophages cultured on SF-BM and IHD exhibited higher secretion levels of the anti-inflammatory cytokines IL-4 and IL-10 with reduced pro-inflammatory cytokine secretion including IL-6 and TNF-α (Fig. 6J-M). Collectively, these findings indicate that IHD effectively attenuated macrophage inflammatory responses.

3.9 IHD inhibits osteoclastogenesis and facilitates cartilage repair

To determine whether IHD-induced macrophage repolarization could influence OA-related osteochondral degeneration, conditioned media from BMMs cultured on different hydrogel surfaces were collected and used to treat osteoclast precursor cells induced with RANKL and M-CSF. Conditioned media from the Gel and HBN groups showed little inhibitory effect on membrane fusion, multinucleated osteoclast formation, F-actin ring formation, or TRAP activity (Fig. 7A-F/I). In contrast, conditioned media from the SF-BM and IHD groups significantly suppressed preosteoclast fusion and osteoclast maturation, with the IHD group showing the strongest inhibitory effect. These results suggest that IHD could inhibit osteoclastogenesis indirectly through macrophage-mediated paracrine regulation.

Chondrocytes are the principal effector cells maintaining cartilage matrix homeostasis, and their reparative activity is strongly shaped by macrophages. Here we assessed whether IHD-reprogrammed macrophages could support cartilage repair by delineating their impact on chondrocytes. Previous studies have shown that M2 macrophage-derived factors such as TGF-β can inhibit osteoclast maturation while promoting chondrogenesis. Based on this notion, conditioned media from macrophages cultured on different hydrogel surfaces were collected for culturing chondrocytes for 7 days. Alcian blue staining showed that chondrocytes treated with conditioned medium from the IHD group produced greater amount of proteoglycan-rich extracellular matrix than the other groups (Fig. 7H). RT-qPCR analysis further showed that cartilage matrix-related genes including ACAN, COL Ⅱ, and SOX9 were upregulated by approximately 4.0-, 3.5-, and 2.0-fold, respectively, whereas the cartilage degradation-related gene MMP13 was downregulated by approximately 3.6-fold in the IHD group (Fig. 7J-M). These findings indicate that IHD-mediated macrophage reprogramming effectively reversed OA-associated cartilage matrix deterioration.

3.10 Evaluation of IHD for OA Treatment In Vivo

To evaluate the therapeutic efficacy of IHD in vivo, a rat OA model was established by anterior cruciate ligament transection (ACLT) for subsequent analysis. Specifically, different hydrogel formulations were injected into the joint cavity after ACLT surgery and administered for 4 weeks. After an additional 8 weeks of incubation, knee joints were collected for therapeutic evaluation (Fig. 8A). According to micro-CT scanning and 3D reconstruction of longitudinal knee sections were first performed to assess subchondral bone changes. As shown in Fig. 8B, samples from the Gel group exhibited typical OA-associated pathological features including rough articular surfaces, severe bone erosion, and marked deterioration of subchondral bone microarchitecture, evidenced by decreased bone mineral density

(BMD), trabecular number (Tb.N), and trabecular thickness (Tb.Th). In contrast, the IHD group showed robust subchondral bone structure that was almost comparable to healthy joints, with bone volume fraction (BV/TV), Tb.N, and Tb.Th increased by 44.6%, 48.2%, and 98.6%, respectively than the Gel group (Fig. 8C-E). Histological analyses based on H&E, Safranin O-Fast Green and Masson staining further confirmed the cartilage-protective effect of IHD. Gel and HBN groups showed severe cartilage degeneration including decreased cartilage thickness, surface erosion, matrix disorganization, and substantial glycosaminoglycan loss (Fig. 8G-I). The SF-BM group partially alleviated cartilage erosion but the effects were modest at most. In contrast, the IHD group displayed a smoother and more continuous cartilage surface, stronger Safranin O staining, and better-preserved tidemark integrity than all the other groups, indicating superior cartilage matrix restoration thereof. Consistently, quantitative evaluation using the Osteoarthritis Research Society International (OARSI) scoring system showed that the Gel group had the highest degeneration score of 22.3/26, whereas the IHD group achieved the lowest score of 9.6/26, followed by the SF-BM group at 14.8/26 (Fig. 8J).

The therapeutic effect of IHD was further validated by immunohistochemical staining of cartilage matrix markers. The Gel group exhibited reduced expression of collagen II and Aggrecan, accompanied by elevated MMP13 expression, reflecting severe cartilage matrix degradation. By contrast, the SF-BM and IHD groups showed increased collagen II and Aggrecan expression and decreased MMP13 expression. Quantitative analysis further confirmed that collagen II and Aggrecan levels were significantly higher in the IHD group than in all other groups (Figure S11). These observations are consistent with the in vitro data and attributable to the in-situ sustained release of Qu-Ca complexes and SDME, which jointly reduce oxidative stress and promote macrophage metabolic reprogramming from glycolysis toward mitochondrial respiration. Indeed, we comparatively analyzed intra-articular ROS levels using dihydroethidium (DHE) staining. As shown in Fig. 8F, ROS signals in the SF-BM and IHD groups were reduced by more than 60% compared with the Gel and HBN groups. Overall, these results demonstrate that IHD effectively abrogates OA-induced osteochondral damage in vivo by coordinated mitochondrial rejuvenation and ROS scavenging.

4. Conclusions

In summary, this study reports a mitochondrion fusion-promoting rejuvenation strategy for OA treatment by developing an injectable hydrogel formulation incorporating biomineralized multifunctional mitochondrial engagers. The IHD hydrogels could be facilely administered to the osteoarthritic joint cavity through intra-articular injection in a minimally invasive manner and release the BMRN in a sustainable manner, which were subsequently internalized by BMMs via size-selective sequestration. The BMRN nanoparticles were efficiently degraded in BMM lysosomes to synchronically release SDME constructs and Qu-Ca complexes. Notably, the SDMEs specifically bridge Cyt C-exposing dysfunctional mitochondria in the intracellular compartment while releasing Mfn1-activating GTP, thereby activating the mitochondrion fusion-dependent endogenous repair programs. Meanwhile, the Qu-Ca complexes ameliorate cellular ROS stress to facilitate mitochondrial maintenance. These effects cooperatively enhance mitochondrial quality control and metabolic fitness, effectively rewiring the bioenergetic

pathways from glycolysis towards OXPHOS to metabolically reprograming BMMs into a pro-regenerative M2-like phenotype. In vivo analysis showed that the IHD treatment substantially improved osteochondral regeneration in osteoarthritic joints on a rat model, offering an approach for improving OA treatment in the clinic.

Declarations

Ethics approval and consent to participate

All animal procedures and protocols were conducted in accordance with the ARRIVE guidelines and were approved by the Animal Ethical and Experimental Committee of the Army Medical University (Chongqing, China) (AMUWEC20255451). All methods were performed in compliance with relevant institutional and national guidelines for the care and use of laboratory animals

Competing interests:

The authors declare no competing interests.

Funding:

This work was supported by the National Natural Science Foundation of China (82402775), Natural Science Foundation of Chongqing (CSTB2024NSCQ-MSX1142, CSTB2025NSCQ-GPX0672), Science and Technology Research Project of Chongqing Education Commission (KJQN202512849), Talent Incubation Program of the Second Affiliated Hospital of Third Military Medical University (2024YQB043)

Author Contribution

Maohua Chen: Data curation, Formal analysis, Investigation, Methodology, Validation, Visualization, Writing – original draft. Fengling Wang: Data curation, Formal analysis, Investigation, Methodology. Xinqiang Hu: Formal analysis, Methodology. Zhenqiang Wang: Formal analysis, Investigation, Methodology. Hao Wei: Formal analysis, Investigation, Methodology. Ming Qin: Investigation, Methodology. Rong Huang: Methodology. Qing Luo: Formal analysis. Zhong Luo: Data curation, Formal analysis, Project administration, Writing – review & editing. Jingbin Huang: Conceptualization, Funding acquisition, Project administration, Supervision.

Acknowledgements

Not applicable

Data availability:

Data is provided within the manuscript or supplementary materials.

References

1. Kloppenburg M, Namane M, Cicuttini F. Osteoarthr Lancet. 2025;405(10472):71–85.
2. Collins KH, Haugen IK, Neogi T, Guilak F. Osteoarthritis as a systemic disease. Nat Rev Rheumatol. 2026;22(2):105–17.
3. Cai C, Wang M, Wang L, Guo J, Wang L, Zhang Y, Wu G, Hua B, Stuart MAC, Guo X, Cao L. Yan, Zwitterionic Brush-Grafted Interfacial Bio-Lubricant Evades Complement C3-Mediated Macrophage Phagocytosis for Osteoarthritis Therapy. Adv Mater. 2025;37(28):2501137.
4. Harasymowicz NS, Harissa Z, Rashidi N, Lenz K, Tang R, Guilak F. Injury and obesity differentially and synergistically induce dysregulation of synovial immune cells in osteoarthritis. Ann Rheum Dis. 2025;84(6):1033–44.
5. Yang X, Tan M, Guo J, Xiang J, Yin F, Deng J, Luo J, Xiao S, Mo M, Wang H, Zhao J, Zheng L, Cheng J, Zhong J. PdZn/CoSA-NC Nanozymes with Highly Efficient SOD/CAT Activities for Treatment of Osteoarthritis via Regulating Immune Microenvironment. Adv Funct Mater. 2024;34(41):2401963.
6. Chen S, Liu X, Zhang W, Li B, Liu F, Zhang Y, Han Y. Nanozyme Coating-Mediated Mitochondrial Metabolic Reprogramming of Macrophages for Immunomodulatory Osseointegration in Rheumatoid Arthritis Case. ACS Nano. 2025;19(28):26127–46.
7. Xue S, Zhao Y, Huang S, Ruan G, Chen J, Huang H, Wu C, Li J, Hu W, Zhang Y, Zhang C, Ding C. A DNA Nanomachine Reverses Mitochondrial Dysfunction by Cascaded Drug Release to Treat Osteoarthritis. Adv Funct Mater. 2025;35(33):2419261.
8. Russell DG, Huang L, VanderVen BC. Immunometabolism at the interface between macrophages and pathogens. Nat Rev Immunol. 2019;19(5):291–304.
9. Tan S, Sun Y, Li S, Wu H, Ding Y. The impact of mitochondrial dysfunction on osteoarthritis cartilage: current insights and emerging mitochondria-targeted therapies. Bone Res. 2025;13(1):77.
10. Zhang Z, Wang X, Fan P, Cheng D, Dang J, Dan X, Xia Y, Fan H. Coupling Mitochondrial Homeostasis to Oxi-Inflamm-Aging Network Disruption via Peptide-Functionalized Nanocomposite Hydrogel for Osteoarthritis Intervention. Adv Mater. 2026;38(24):e11804.
11. Li H, Yuan Y, Zhang L, Xu C, Xu H, Chen Z. Reprogramming Macrophage Polarization, Depleting ROS by Astaxanthin and Thioketal-Containing Polymers Delivering Rapamycin for Osteoarthritis Treatment. Adv Sci. 2024;11(9):2305363.
12. Liu Y, Duan J, Dang Y, Hao R, Wang H, Tan E, Wang R, Li Y, Zhang S, Wang Y, Lv J, Qi Y, Zhang X, Cheng Y. Remodeling of senescent macrophages in synovium alleviates trauma- and aging-induced osteoarthritis. Bioactive Mater. 2026;55:42–56.
13. Zu X, Chen S, Li Z, Hao L, Fu W, Zhang H, Yin Z, Wang Y, Wang J. SPI1 activates mitochondrial unfolded response signaling to inhibit chondrocyte senescence and relieves osteoarthritis. Bone Res. 2025;13(1):47.

14. Zhang L, Chen X, Cai P, Sun H, Shen S, Guo B, Jiang Q. Reprogramming Mitochondrial Metabolism in Synovial Macrophages of Early Osteoarthritis by a Camouflaged Meta-Defensome. Adv Mater. 2022;34(30):2202715.
15. Ryu KW, Fung TS, Baker DC, Saoi M, Park J, Febres-Aldana CA, Aly RG, Cui R, Sharma A, Fu Y, Jones OL, Cai X, Pasolli HA, Cross JR, Rudin CM, Thompson CB. Cellular ATP demand creates metabolically distinct subpopulations of mitochondria. Nature. 2024;635(8039):746–54.
16. Hong X, Isern J, Campanario S, Perdiguero E, Ramírez-Pardo I, Segalés J, Hernansanz-Agustín P, Curtabbi A, Deryagin O, Pollán A, González-Reyes JA, Villalba JM, Sandri M, Serrano AL, Enríquez JA. Muñoz-Cánoves, Mitochondrial dynamics maintain muscle stem cell regenerative competence throughout adult life by regulating metabolism and mitophagy. Cell Stem Cell. 2022;29(9):1298–e131410.
17. Madhu V, Hernandaz-Meadows M, Coleman A, Sao K, Inguito K, Haslam O, Boneski PK, Sesaki H, Barve RA, Collins JA, Risbud MV. The loss of OPA1 accelerates intervertebral disc degeneration and osteoarthritis in aged mice. Nat Commun. 2025;16(1):5996.
18. Tábara LC, Burr SP, Frison M, Chowdhury SR, Paupe V, Nie Y, Johnson M, Villar-Azpillaga J, Viegas F, Segawa M, Anand H, Petkevicius K, Chinnery PF, Prudent J. MTFP1 controls mitochondrial fusion to regulate inner membrane quality control and maintain mtDNA levels. Cell. 2024;187(14):3619–e363727.
19. Shao Y, Zhang H, Guan H, Wu C, Qi W, Yang L, Yin J, Zhang H, Liu L, Lu Y, Zhao Y, Zhang S, Zeng C, Wang G, Bai X, Cai D. PDZK1 protects against mechanical overload-induced chondrocyte senescence and osteoarthritis by targeting mitochondrial function. Bone Res. 2024;12(1):41.
20. Yang W, Feng Z, Lai X, Li J, Cao Z, Jiang F, Chen F, Zhan S, Kong F, Yang L, Teng Y, Watford WT, Zhou G, Xie J. Calcium nanoparticles target and activate T cells to enhance anti-tumor function. Nat Commun. 2024;15(1):10095.
21. Duchstein P, Schodder PI, Leupold S, Dao TQN, Kababya S, Cicconi MR, de Ligny D, Pipich V, Eike D, Schmidt A, Zahn D, Wolf SE. Small-Molecular-Weight Additives Modulate Calcification by Interacting with Prenucleation Clusters on the Molecular Level. Angew Chem Int Ed. 2022;61(40):e202208475.
22. Li Z, Deng X, Qiu C, Wang Z, Tang F, Pi Y, He Z, Zheng C, Luo J. Orally administered degradable nanoarmor-assisted probiotics for remodeling the gut microenvironment and treating osteoporosis. J Nanobiotechnol. 2025;23(1):660.
23. Zhang H, Feng H, Ling J, Ouyang X-k, Song X. Enhancing the stability of zein/fucoidan composite nanoparticles with calcium ions for quercetin delivery. Int J Biol Macromol. 2021;193:2070–8.
24. He X, He S, Xiang G, Deng L, Zhang H, Wang Y, Li J, Lu H. Precise Lubrication and Protection of Cartilage Damage by Targeting Hydrogel Microsphere. Adv Mater. 2024;36(40):2405943.
25. Long D, Mao G, Li H, Chen H, Huang R, Zhao T, Zhang Z, Zhao X. Injectable Nanocomposite Hydrogel System for miRNA-Based Cartilage Repair in Knee Osteoarthritis. Adv Funct Mater. 2025;35(39):2423227.

26. Nguyen DD, Barulin A, Yu WJ, Park J-C, Kim I. Coincident Fluorescence-Burst Analysis of Actin Cargo Molecules in Secreted Single Diffusing Extracellular Vesicles From Human Induced Pluripotent Stem Cells. Adv Sci. 2026;13(13):e14421.
27. Dong C, Ren J. Resonance Light-Scattering Correlation Spectroscopy and Its Application in Analytical Chemistry for Life Science. Acc Chem Res. 2023;56(19):2582–94.
28. Li Z, Wu B, Li W, Marsili E, Tang K, Sun K, Cao Z, Zhang Y, Huang H, Li X, Wang G. Unlocking an Efficient SOD-to-CAT Catalytic Relay in a MOF Nanozyme via Dopamine-Driven Interfacial Nanoreconstruction for Osteoarthritis Therapy. Adv Mater. 2026;38(19):e72747.
29. Ou Z, Wei J, Lei J, Wu D, Tong B, Liang H, Zhu D, Wang H, Zhou X, Xu H, Du Z, Du Y, Tan L, Yang C, Feng X. Biodegradable Janus sonozyme with continuous reactive oxygen species regulation for treating infected critical-sized bone defects. Nat Commun. 2024;15(1):10525.
30. Chen T, Wang X, Zhang G, Wang L, Wan J, Tan L, Fan X, Meng S, Jin Z, Liang Y, Li H, Wan Z, Xu X, Zhang Y, Qin L, Malashicheva A, Du Y, Zang G, Wang G. Curcuminoids amplify host innate antiviral immunity via the CRYAB-RBM26 axis in viral infection, iMeta 5(1) (2026) e70111.

Figures

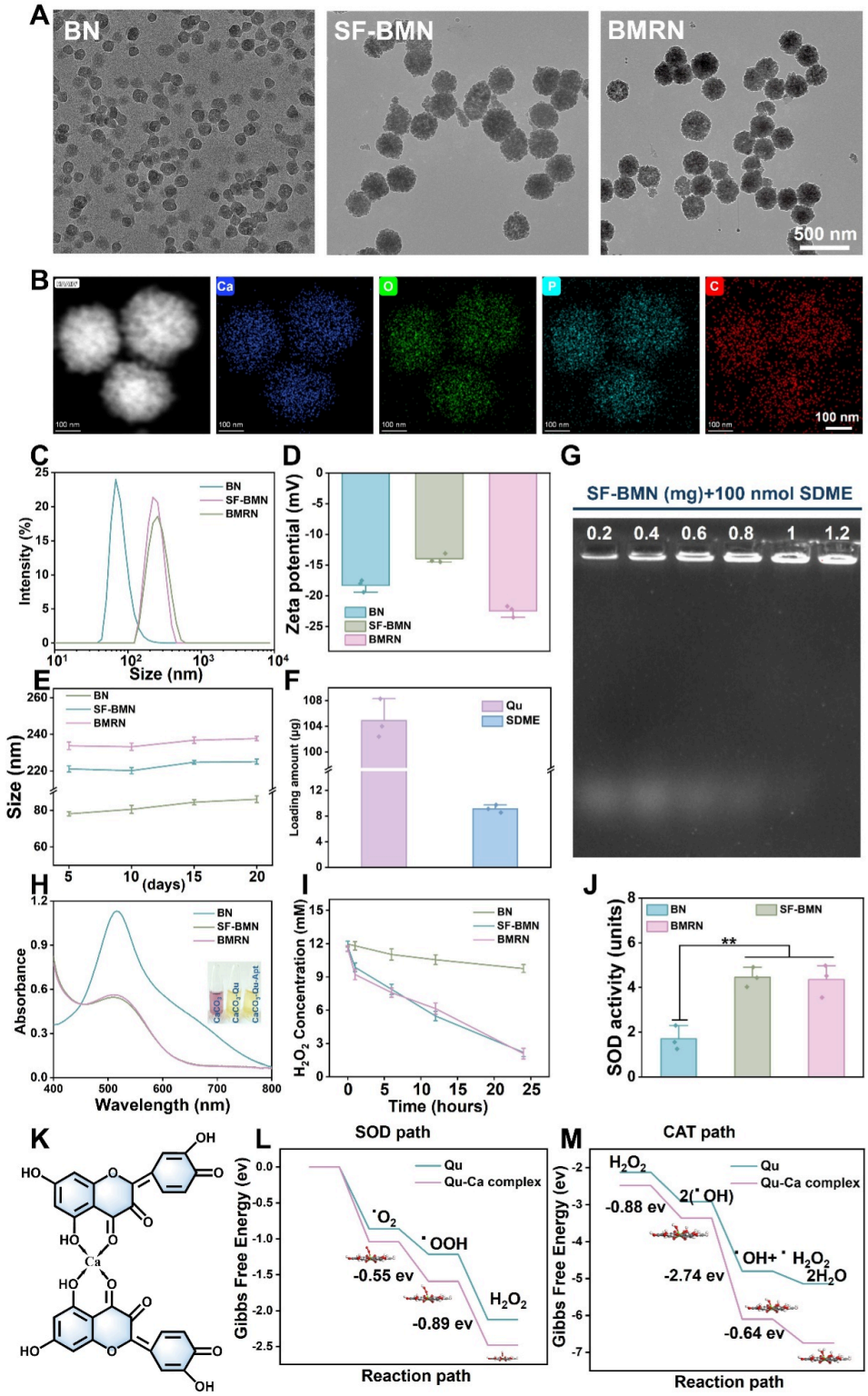


Figure 1

Fabrication and characterization of BMRNs. (A)TEM images of BNs, SF-BMNs and BMRNs; (B) EDS images of BMRNs; (C) DLS analysis the size distribution of BNs, SF-BMNs and BMRNs; (D) Zeta potential of BNs, SF-BMNs and BMRNs; (E) Time-dependent size changes of different nanoparticles; (F) The loading amount of quercetin and SDME in BMRNs; (G) The loading amount of SDME in different dosage of BMRNs; (H) Total ROS scavenging activity of different nanoparticles through DPPH reaction; (I)CAT

and (J) SOD activity detection in different nanoparticles; (K) The structural formula of Qu-Ca complex; The reaction energy diagrams of simulated (L) SOD-like and (M) CAT-like processes on Qu-Ca complex. Data were presented as mean ± SD for $n = 3$, $^{*}p < 0.05$, $^{**}p < 0.01$.

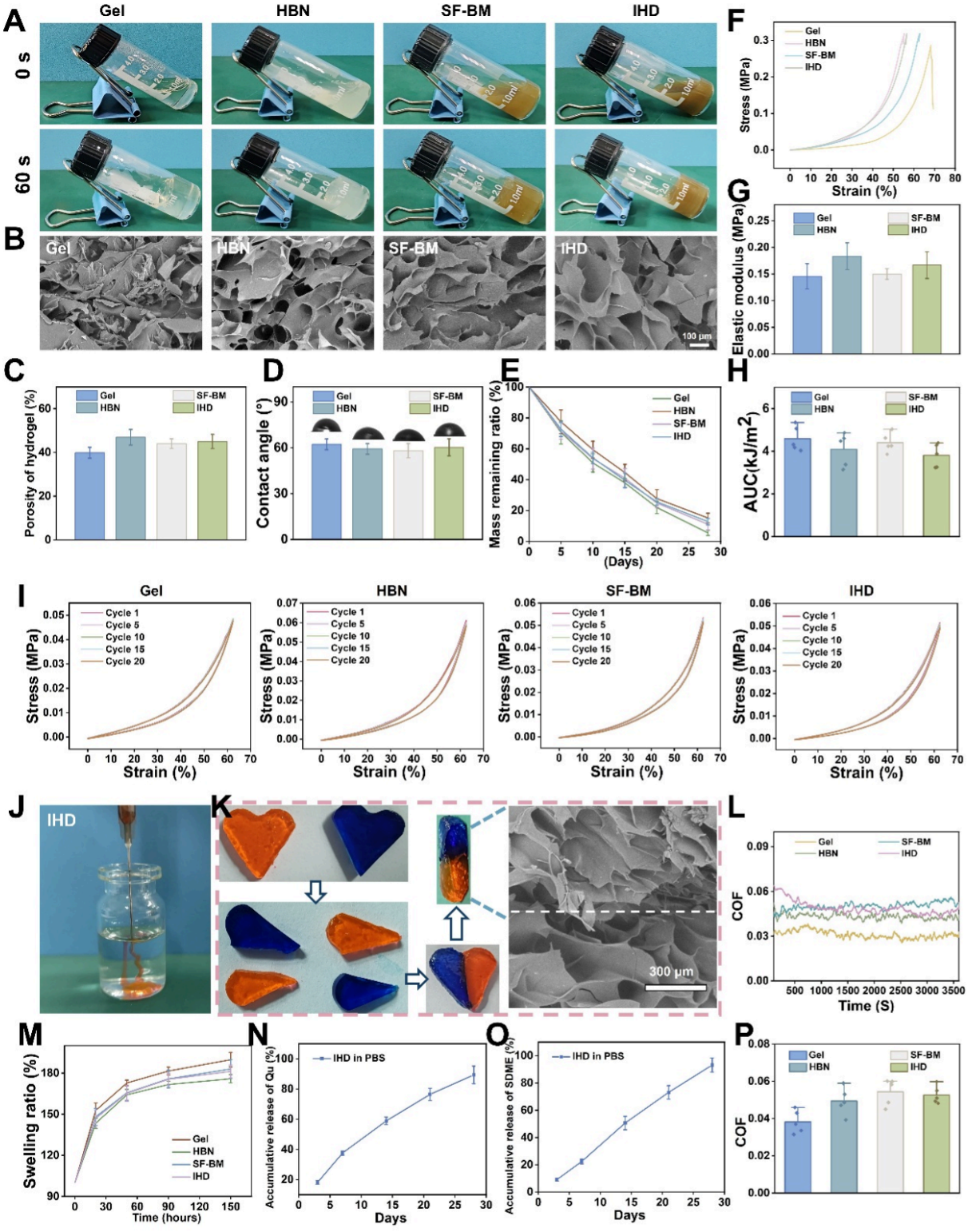


Figure 2

IHD fabrication and characteristics of mechanical, tribological and degradation properties. (A) The process of preparing IHD hydrogel; (B) SEM images of different hydrogels; (C) The porosity, (D) contact angle and (E) degradation properties of different hydrogels; (F) The compressive strain-stress curve of different hydrogels; (G) Elastic modulus and (H) AUC of different hydrogels; (I) The cyclic compressive strain-stress curve of different hydrogels; (J) The formation of the injectable IHD hydrogel; (K) The Self-healing of IHD hydrogel; (L) Representative friction coefficient versus time profiles for Gel, HBN, SF-BM and IHD hydrogels; (M) Swelling ration of different hydrogels; Release profiles of (N) Qu and (O) SDME from IHD; (P) Quantitative statistics of friction coefficients in different hydrogels. Data were presented as mean ± SD for $n = 5$, *$p < 0.05$, **$p < 0.01$.

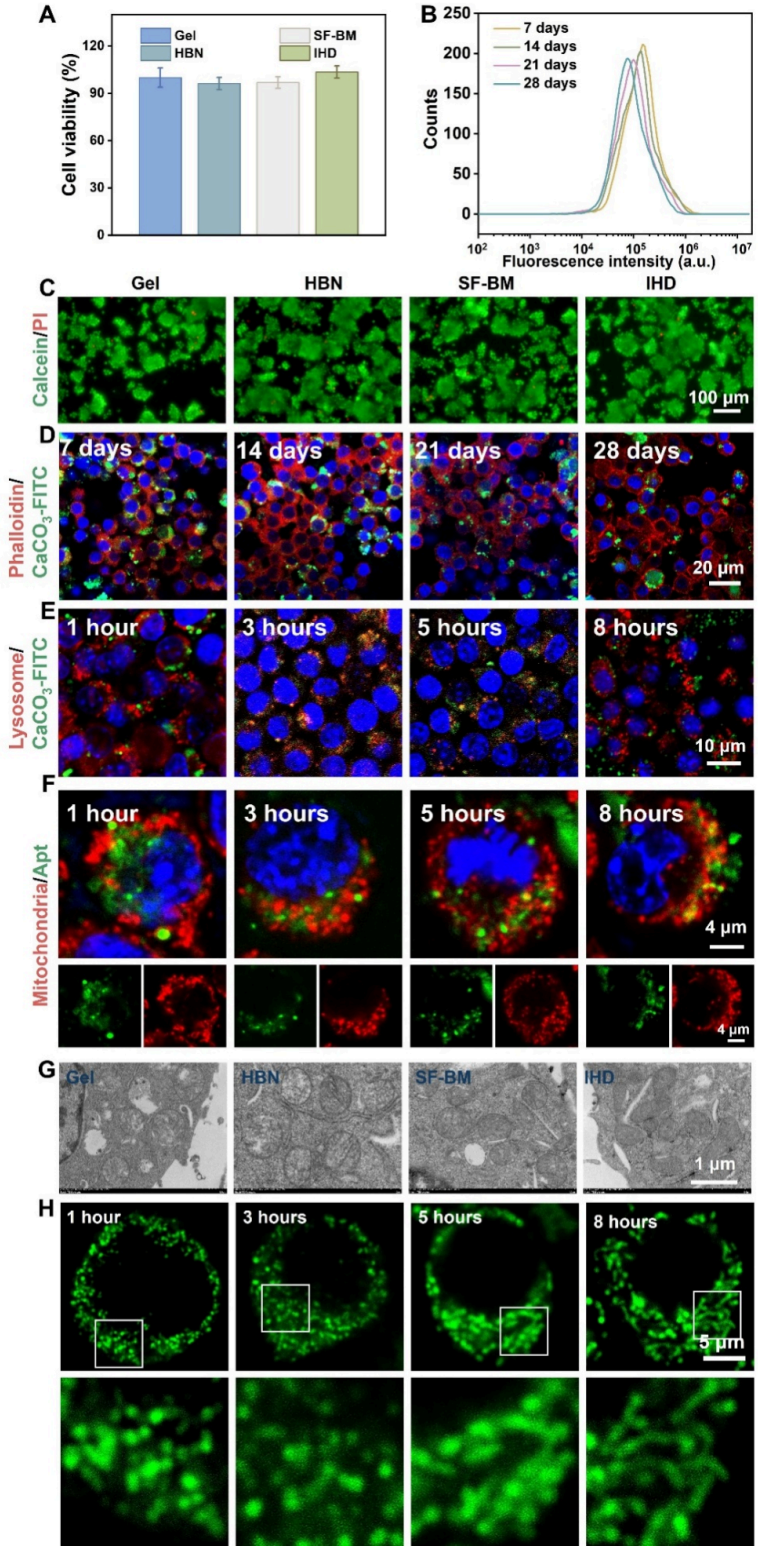


Figure 3

Biocompatibility and mitochondrial repair function of IHD. (A) Viability of BMMs cultured on different hydrogels by cck-8 testing kit; (B) Uptake analysis of BMRN-FITC by BMMs via flow cytometer; (C) Live/dead staining of BMMs cultured on different hydrogels; (D) CLSM images of BMMs cultured for 24 hours with different incubation media. Blue fluorescence: cell nucleus, red fluorescence: cell membrane, and green fluorescence: BMRN-FITC, respectively; (E) CLSM images of BMMs cultured for 1, 3, 5 and 8h

with IHD-FITC incubation media. The blue, red, and green colors indicate cell nucleus, lysosome, and the fluorescein-labeled BMRN, respectively. (F) Fluorescence co-localization of SDME and mitochondria in macrophages; (G) TEM images of the mitochondrial structures in macrophages cultured on different hydrogel; (H) Mitochondrial staining with Mito-Tracker Green after various treatment. Data were presented as mean ± SD for $n = 3$, *$p < 0.05$, **$p < 0.01$.

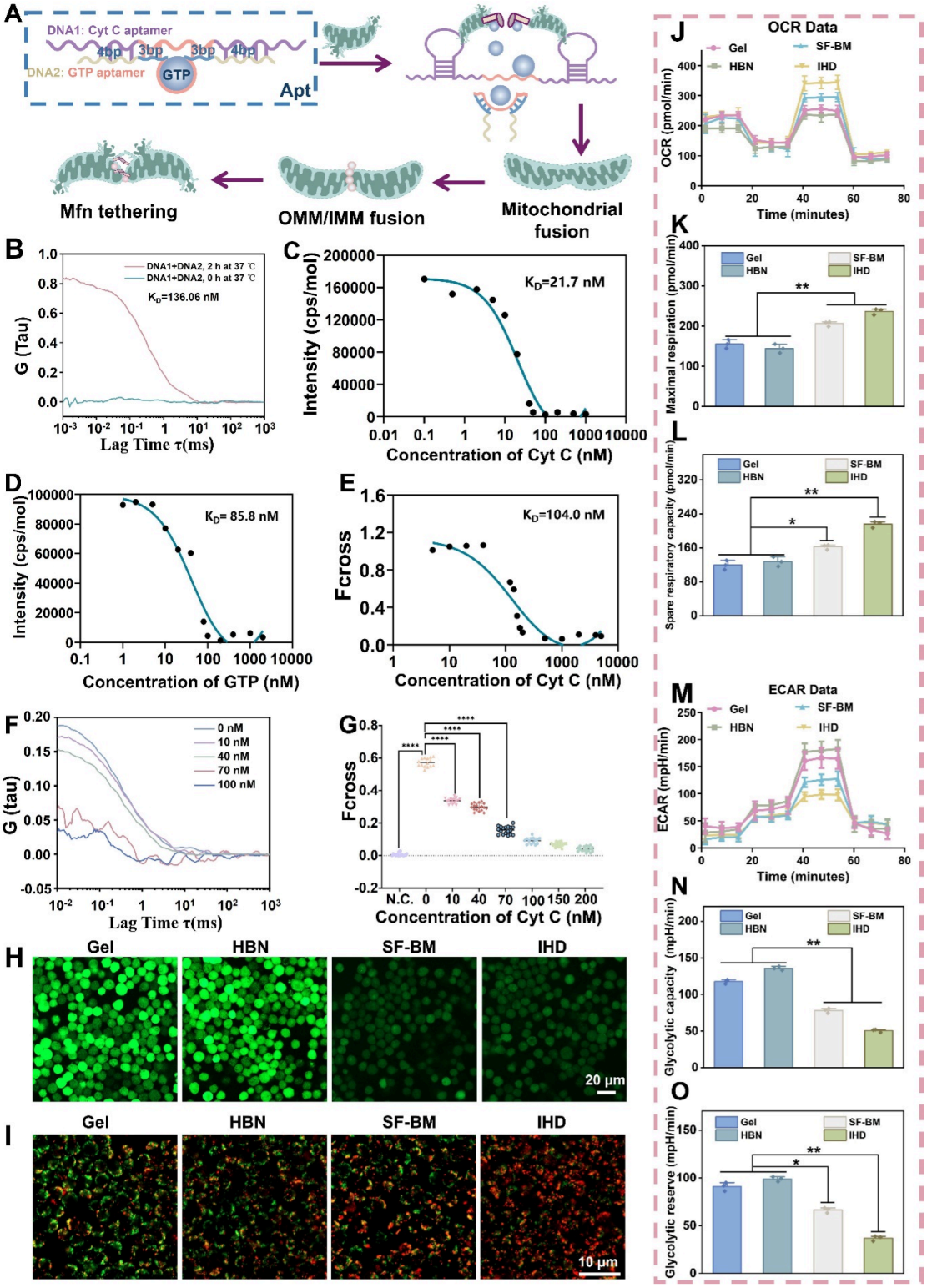


Figure 4

IHD-induced metabolic reprogramming in macrophages. (A) A schematic illustration depicts the process by which SDME induces mitochondrial fusion; (B) Fluorescence colocalization analysis for assessing DNA1 and DNA2 complexation; (C) The affinity of DNA1 for Cyt C; (D) The affinity of DNA2 for GTP; (E) The affinity of duplex SDME for Cyt C; (F) The cross-correlation curve of DNA1 and DNA2 in the presence of Cyt C; (G) Cyt C concentration-dependent dissociation of duplex SDME; (H) The intracellular ROS levels of BMMs via CLSM observation; (I) JC-1 staining for assessing the mitochondrial membrane potential in BMMs cultured on different hydrogels; (J-L) OCR detection via cell Mito Stress test kits for analyzing maximal respiration and spare respiratory capacity; (M-O) ECAR detection via cell Mito Stress test kits from Agilent, with glycolytic capacity and glycolytic reserve. Data were presented as mean ± SD for $n = 3$, *$p < 0.05$, **$p < 0.01$.

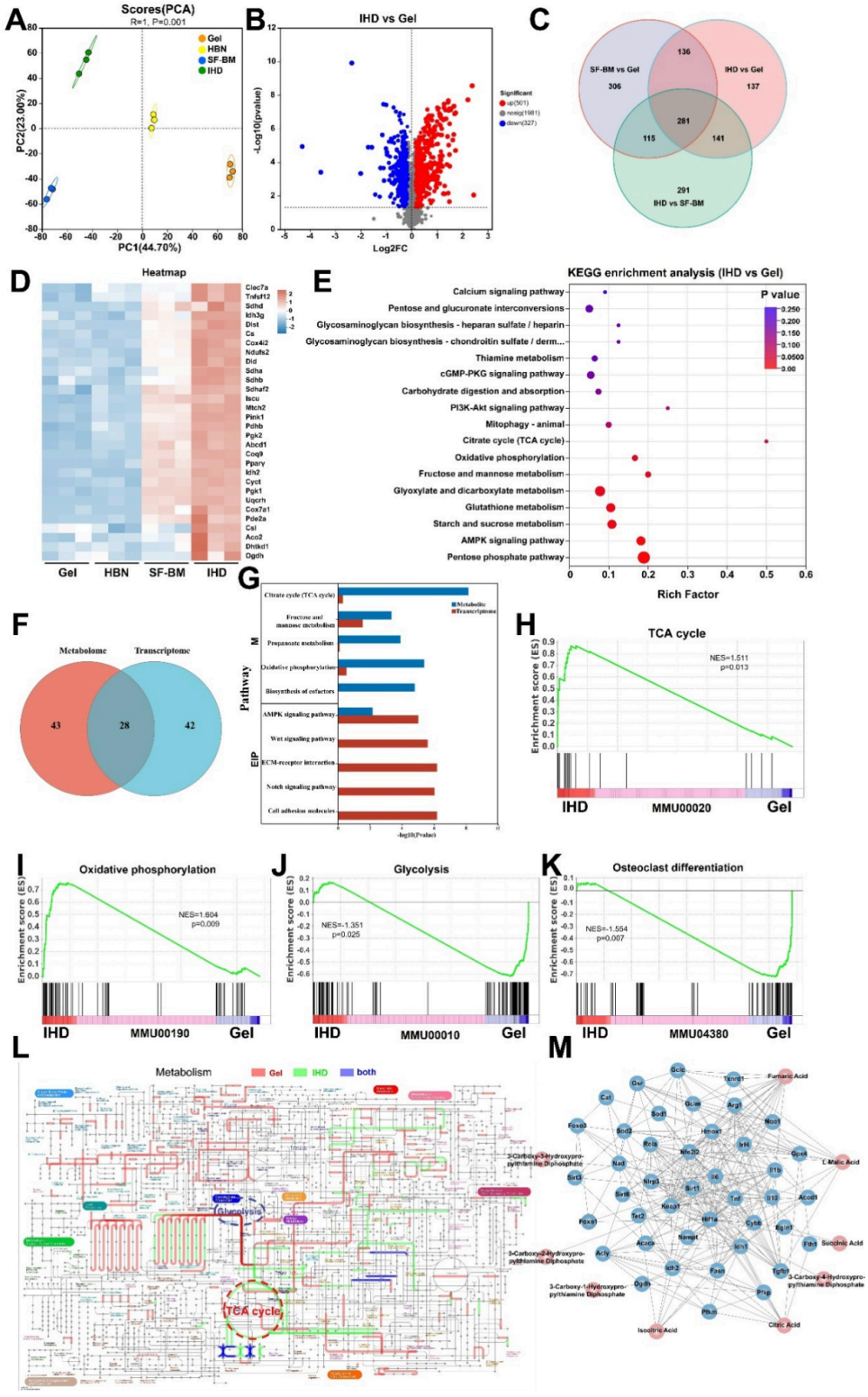


Figure 5

IHD hydrogels initiate the macrophage metabolic reprogramming. (A) principal component analysis of macrophage metabolites from different groups; (B) Volcano plot representing the comparison of metabolites in BMMs cultured on IHD and Gel surface; (C)Wayne's analysis of differentially metabolites between the Gel, HBN, SF-BM and IHD; (D) Heat map of upregulated and downregulated metabolism-related genes in each group; (E) Up-regulated KEGG pathway analysis of IHD group; (F) Wayne's analysis

of up-regulated gene and metabolites; (G) KEGG annotations analysis gene and metabolite enriched signaling pathway; (H-K) GSEA of TCA cycle, oxidative phosphorylation, glycolysis, osteoclast differentiation, and heatmap of core enrichment symbols; (L) Metabolic profiling of the IHD and Gel groups; (M) Interaction network of metabolites and anti-inflammatory and anti-oxidation related genes.

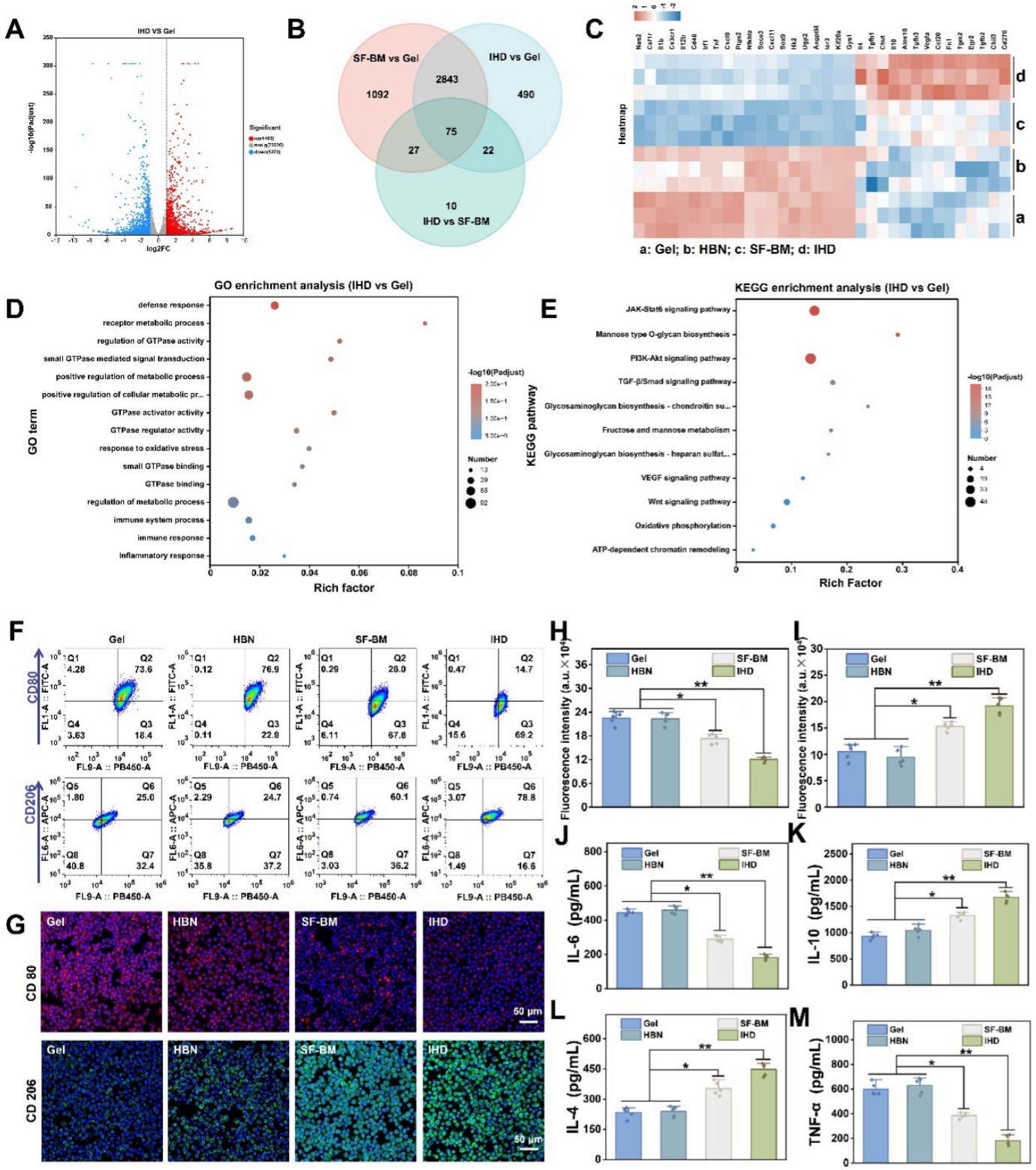


Figure 6

IHD induces macrophage polarization from proinflammatory M1 to the anti-inflammatory M2 phenotype. (A) Volcano plot representing the comparison of gene expressions in macrophages cultured on IHD and Gel surface. Upregulated genes are marked in red and downregulated genes are marked in blue; (B) Wayne's analysis of differentially gene expressions between the Gel, HBN, SF-BM and IHD; (C) Heat map of upregulated and downregulated inflammation-related genes in each group; Up-regulated (D) GO and (E) KEGG pathway analysis of IHD group; Detection of CD 80 and CD 206 expression in macrophage via (F) flow cytometer and (G) CLSM; Quantitative analysis the fluorescence intensity of (H) CD80 and (I) CD206; (J-K) The effects of IHD on IL-6/IL-10/IL-4/TNF-α expression in macrophages. Data were presented as mean ± SD for $n = 5$, *$p < 0.05$, **$p < 0.01$.

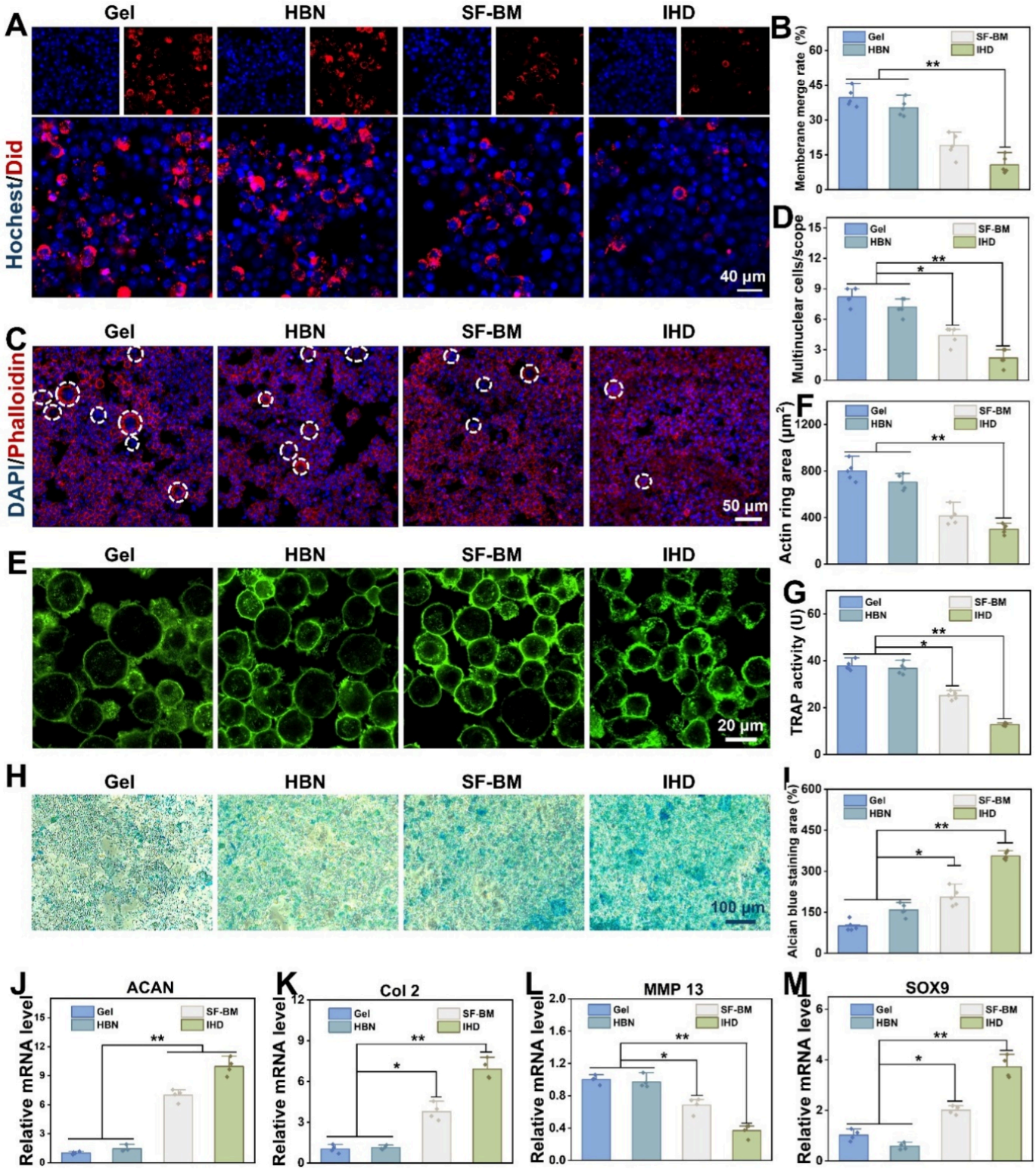


Figure 7

IHD inhibits osteoclastogenesis and facilitates chondrogenesis. (A) CLSM observation osteoclast fusion and (B) statistical analysis of cell membrane fusion rates, data were presented as mean ± SD for $n = 5$, *$p < 0.05$, **$p < 0.01$; (C) CLSM images and (D) quantitative analysis the number of multinucleated cells, data were presented as mean ± SD for $n = 5$, *$p < 0.05$, **$p < 0.01$; (E) CLSM images and (F) quantitative analysis of cellular F-actin rings, data were presented as mean ± SD for $n = 5$, *$p < 0.05$, **$p < 0.01$; (G)

TRAP activity, data were presented as mean ± SD for $n = 5$, *$p < 0.05$, **$p < 0.01$; (H) Alcian blue staining and (I) quantitative analysis the deposition of ECM for different groups, data were presented as mean ± SD for $n = 5$, *$p < 0.05$, **$p < 0.01$; (J-M) RT-qPCR assays of marker gene expression for chondrogenesis, data were presented as mean ± SD for $n = 4$, *$p < 0.05$, **$p < 0.01$.

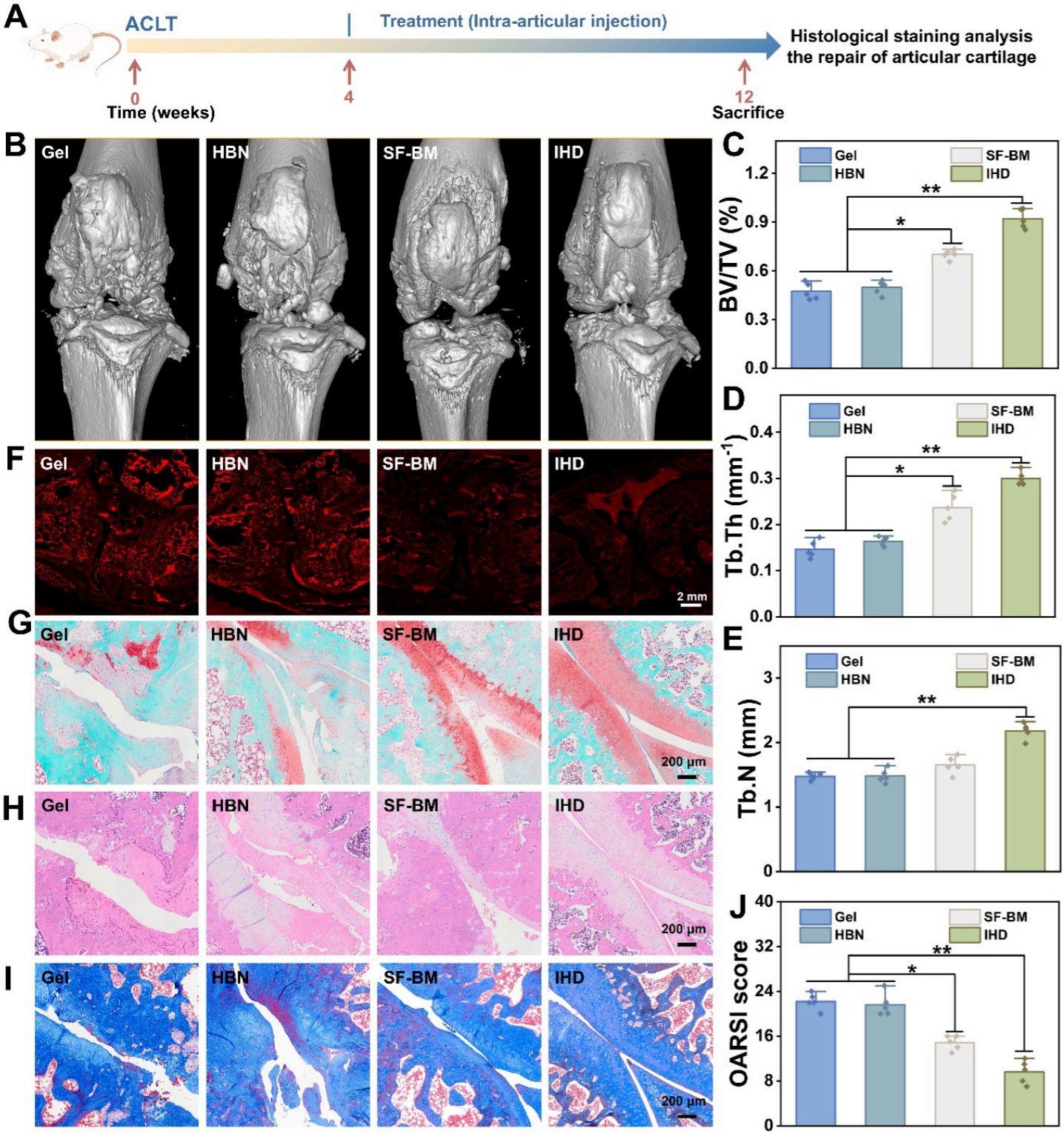


Figure 8

In vivo evaluation the therapeutic efficacy IHD in OA rat model. (A) Schematic illustration of the animal model construction and operation procedures; (B) Representative Micro-CT images of the knee joints after 8 weeks of joint cavity injection with different hydrogels. (C-E) Quantitative analysis of BV/TV, Tb.Th and Tb.N; (F) In vivo ROS staining by IDH of rat joints; (G) Safranin O-fast green, (H) H&E and (I) Masson staining of rat knee joint tissues in different groups; (J) OARSI score of the repair areas of different groups. Data were presented as mean ± SD for $n = 5$, $^{*}p < 0.05$, $^{**}p < 0.01$.

Supplementary Files

This is a list of supplementary files associated with this preprint. Click to download.

- SupportingInformation.docx
- floatimage1.jpeg